 CMES, vol.73, no.2, pp.137-169, 2011

Motion of Small Solid Particles in a Viscous Fluid Enclosed in a Cavity

L. Hedhili, A. Sellier, L. Elasmi and F. Feuillebois

Abstract: The motion of a solid particle embedded in a viscous fluid in a closed container requires a precise account of wall effects when in creeping flow. The boundary integral method, which amounts to solving a Fredholm integral equation for the stress on the particle and walls, is used here. The accuracy of the method is improved by using curvilinear six-node triangular boundary elements, the size of which is specially adapted to the particle shape and position with respect to walls. The method is applied to resolve the case of a moving particle in a parallelepiped container. It is validated by comparing with earlier analytical results for a sphere interacting with two parallel or perpendicular walls and with numerical results for a sphere in the center of a cubic container. Results are then provided for a spherical and an ellipsoidal particle, both either with imposed motion or settling in a cubic container.

Keywords: Stokes flow, wall-particle interactions, cubic cavity, sedimentation, Green tensor, boundary-integral equations.

1 Introduction

The motion of small solid particles in a viscous fluid enclosed in a cavity is of interest for various applications at microscales, such as microfluidic devices, laboratories on chips, biology (e.g. particles in lungs and in blood vessels). At these scales, the Reynolds number based on the particle size a and characteristic velocity V relative to the fluid is usually low compared with unity: $Re = aV/\nu \ll 1$, where ν is the kinematic viscosity. Then the unsteady Navier-Stokes equations for the fluid motion simplify in the first approximation $Re \to 0$ to the steady Stokes equations for inertialess fluid motion. Solutions of these equations have been the topic of a large body of literature since the seminal work of Stokes (1851). The Green function of Stokes equations in unbounded fluid, also called the Stokeslet after Hancock (1953), is the flow field due to a point force applied to the viscous fluid. The Stokeslet fluid velocity decays as the inverse of the distance to the point force,

so that all hydrodynamic interactions are long-ranged. As a consequence, all walls surrounding the fluid have a significant influence. When the whole fluid is enclosed in a cavity, all walls may then widely modify the flow field. This is the incentive for the present paper. Another peculiar property of Stokes equations is the lubrication effect: when a particle approaches a wall so that the gap becomes small compared with the particle dimension, expelling the viscous fluid requires a force which increases like the inverse of the gap. The difficulty then is to calculate accurately the large variations in stress in the gap. The literature is huge, even when restricting the focus to wall effects in Stokes flow. Thanks to the linearity of Stokes equations, a number of analytical - exact or even approximate - solutions exist. Many such solutions are provided in textbooks and review articles (e.g. Berker (1963); Happel and Brenner (1991); Kim and Karrila (1991); Feuillebois (1989)). Only a few landmarks will be recalled here. Lorentz (1897), then Faxen (1924) provided approximate solutions for the force on a spherical particle at some distance from one and two walls. The Green function of Stokes equations in a fluid domain limited by a plane wall was obtained later by Blake (1971). Analytical solutions for the case of a sphere near a wall were obtained by the method of bispherical coordinates. Various results may be found in Brenner (1961); Maude (1961); Dean and O'Neill (1963); O'Neill (1964, 1967, 1968); Cooley and O'Neill (1969); O'Neill (1969). More recently, it was proven that this method may provide accurate results even for a small gap between a sphere and a plane wall (see Chaoui and Feuillebois (2003); Pasol, Chaoui, Yahiaoui, and Feuillebois (2005); Pasol, Sellier, and Feuillebois (2006)). A review of these recent papers is given in Pasol, Sellier, and Feuillebois (2009). The Green function of Stokes equations in presence of parallel walls, albeit more complicated, was found in different forms by Vasseur and Cox (1976) (Sec. 3), Liron and Mochon (1976) and Jones (2004). Results for a sphere interacting with two perpendicular walls, or more generally with a wedge, were obtained by Sano and Hasimoto (1976, 1977); Sano (1978). Results for a cylindrical container exist, either when open, starting with the early work of Faxen (1922-1923), or closed at both ends. The Green function for a point force located on the cylinder axis in this case was found by Blake (1979) (see also Sano (1987)). In the frame of analytical or semi-analytical methods, the multipoles method has the advantage of providing results for several interacting spheres (see Cichocki, Felderhof, Hinsen, Wajnryb, and Bławzdziewicz (1994)), even in the presence of two parallel walls (see Bhattacharya, Bławzdziewicz, and Wajnryb (2005)). A good review of the method is presented in Ekiel-Jeżewska and Wajnryb (2009). By comparison, works concerned with a closed container are relatively less numerous. A spherical container can be considered simply as another spherical particle in the calculation. Thus, the bispherical coordinates method may be applied (see Jones (2009)). By also considering a spherical container as a sphere among other ones, the interac-

tions of two spheres in a spherical container were taken into account by Beenakker and Mazur (1985). They used an earlier method akin to the multipoles method, albeit more complicated. Therefore, this method could practically only provide a few terms of asymptotic expansions of particle mobilities for large distances compared with a particle radius. The case of a closed rectangular container was considered by Shankar (2007) who obtained solutions as series for lid driven flows. However, the Green function for the rectangular container is still too difficult to tackle, to our knowledge. When the geometry becomes increasingly complicated, the analytical or semi-analytical solutions become increasingly cumbersome and eventually not feasible. Numerical solutions are then appropriate. General numerical methods (finite elements method, fine volumes method, finite differences) may be applied to Stokes equations, like for the more general Navier-Stokes equations. But since Stokes equations are linear, it proves more efficient to exploit this property by using analytical-numerical types of solutions. For instance, for a sphere moving along the axis of a cylindrical container close at both ends, Lecoq, Masmoudi, Anthore, and Feuillebois (2007) used solutions of Stokes equations as series adapted to the cylindrical geometry and applied the no-slip condition on the moving sphere in the sense of least squares. In three dimensions, various analytical-numerical methods use distributions of Stokeslets. For instance, the method of fundamental solution (see Debbech, Elasmi, and Feuillebois (2010) and references therein; the method in this context is also called the singularity method) consists in expressing the flow field in terms of Stokeslets and its derivatives positioned at chosen points outside of the fluid domain. But the most widely used method based on the Green function is the boundary integral method, probably initiated by Youngren and Acrivos (1975, 1976) and used in a number of papers even since. The method consists in distributing Stokeslets on the particles surfaces and adjusting their intensities so as to enforce the proper boundary conditions on surfaces. When in presence of walls with simple geometries, it is often more efficient to use the appropriate Green function which satisfies automatically the boundary condition on walls (e.g. Blake (1971) Green function for one wall and Jones (2004) for two parallel plane walls); this technique was applied in Pasol and Sellier (2006) to determine the motion of a two-particle cluster between parallel walls. In the case of a closed cavity of any shape, the Green function is unknown, except for a spherical cavity (see Sellier (2008)). It is then necessary to distribute Stokeslets on all surfaces, that is on particles and on the walls of the cavity. As compared with the classical numerical methods quoted above (finite elements, etc.), only surfaces have to be meshed here. This restriction provides a tremendous gain in rapidity and also improved accuracy over the classical methods in which the whole fluid domain has to be meshed. This is here the incentive for using the boundary integral method. The refinements proposed in the present paper aim at increasing the precision of this method, in particu-

lar for close surfaces. First, the seldom used 6-node curvilinear triangular boundary elements are prefered. Then, because of lubrication, it appears necessary to refine and adapt the mesh in the gap between a particle and the wall, so as to describe with sufficient accuracy the rapidly varying stresses which apply on the surfaces in this region. The improvements provided by these refinements are illustrated on the case of particles moving in a rectangular cavity. This type of container is ubiquitous in man-made applications. The paper is organized as follows. First the assumptions and relevant boundary integral formulation are presented in §2.Then, the proposed numerical strategy and carefully selected benchmarks are addressed in §3. Section 4 is devoted to numerical results, both for spherical and ellipsoidal particles. Some results are compared with previous works and with those obtained with a commercial finite elements software (Comsol). Finally conclusions are drawn in §5.

2 Governing problem and proposed boundary formulation

This section first presents the assumptions and addressed problems. It then introduces the boundary formulation and associated boundary-integral equations to be solved.

2.1 Assumptions and addressed problems

Consider, as depicted in Figure 1, a solid particle $\mathscr{P}$ with center of mass O_1, uniform density ρ_s, volume $\mathscr{V}$ and boundary S. The particle shape should be smooth, but otherwise may in principle be arbitrary.

The particle is immersed in a Newtonian fluid with uniform viscosity $\mu > 0$ and density $\rho > 0$ confined in a closed cavity with surface Σ. A Cartesian coordinates system (O, x_1, x_2, x_3) is attached to the cavity. On the fluid boundary $S \cup \Sigma$, a unit normal vector $\mathbf{n}$ points into the fluid domain $\mathscr{D}$. The particle is submitted to a uniform gravity field $\mathbf{g}$ and moves as a rigid body with a translational velocity $\mathbf{U}$ (the velocity of O_1) and an angular velocity $\pm\Omega$. The fluid pressure is written as $p + \rho \mathbf{g}.\mathbf{x}$, where p is the dynamic pressure and $\mathbf{x}$ a position vector, and its velocity is $\mathbf{u}$ (with typical magnitude V). Let the particle length scale be a (for a sphere, we take its radius). The particle is small enough for the Reynolds number $\mathrm{Re} = \rho V a/\mu$ to be low as compared with unity. In the first approximation, fluid inertia may be neglected and the flow $(\mathbf{u}, p)$ is described by the steady Stokes equations:

$$\mu \nabla^2 \mathbf{u} = \nabla p \,, \quad \nabla \cdot \mathbf{u} = \mathbf{0} \ \text{ in } \mathscr{D}. \tag{1}$$

The no-slip boundary condition for the velocity applies on each solid surface:

$$\mathbf{u} = \mathbf{U} + \pm\Omega \wedge \mathbf{r} \text{ on } S \,, \quad \mathbf{u} = \mathbf{0} \text{ on } \Sigma \,, \tag{2}$$

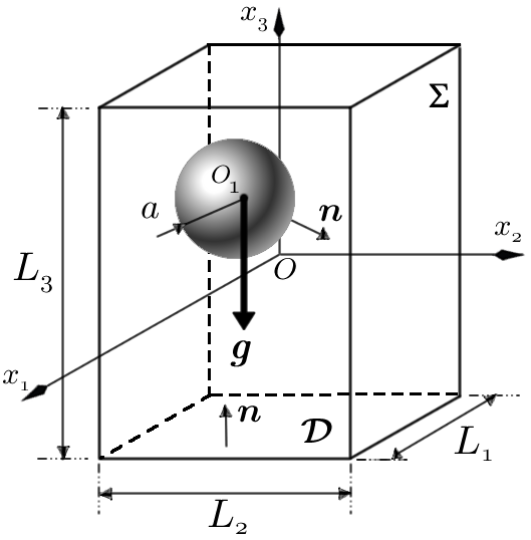

Figure 1: A moving solid particle $\mathscr{P}$ in a motionless cavity Σ.

where $\mathbf{r}$ is a position vector originating from O_1. The flow $(\mathbf{u}, p)$ with stress tensor $\pm\sigma$ exerts on the particle a force $\mathbf{F}$ and a torque $\mathbf{T}$ (about O_1) given by

$$\mathbf{F} = \int_S \pm\sigma\cdot\mathbf{n}\,dS, \qquad \mathbf{T} = \int_S \mathbf{r}\wedge\pm\sigma\cdot\mathbf{n}\,dS. \tag{3}$$

At this stage $\mathbf{U}, \pm\Omega, \mathbf{F}, \mathbf{T}$ are unknown but related through the flow field. We consider here the two cases introduced in the following subsections.

2.1.1 Case 1: prescribed particle rigid-body motion

In this case, the velocities $(\mathbf{U}, \pm\blacksquare)$ are prescribed. As shown in Pozrikidis (1992), the problem (1)-(2) then has a unique solution. From linearity of Stokes equations (1), it is also convenient to introduce six auxiliary Stokes flows $(\mathbf{u}_T^{(i)}, p_T^{(i)})$ and $(\mathbf{u}_R^{(i)}, p_R^{(i)})$ with $i = 1,2,3$, which are solutions of (1) with the specific boundary conditions:

$$\mathbf{u}_T^{(i)} = \mathbf{0}, \quad \mathbf{u}_R^{(i)} = \mathbf{0} \qquad \text{on } \Sigma, \tag{4a}$$

$$\mathbf{u}_T^{(i)} = \mathbf{e}_i, \quad \mathbf{u}_R^{(i)} = \mathbf{e}_i\wedge\mathbf{r} \qquad \text{on } S. \tag{4b}$$

In other words, these flows are produced when the particle either translates or rotates at the unit dimensionless velocity $\mathbf{e}_i$. Such a convenient choice is standard in this intermediate mathematical step (see, for instance, Happel & Brenner [21]),

but care should be taken about dimensions: $\mathbf{u}_T^{(i)}$ is dimensionless, $\mathbf{u}_R^{(i)}$ is in metres; then, for consistency with (1), $p_T^{(i)}$ is in Pa.s/m and $p_R^{(i)}$) is in Pa.s.

For $L=T$ or $L=R$ and $i=1,2,3$ we introduce the stress tensor $\pm\boldsymbol{\sigma}_L^{(i)}$ associated to the flow field $(\mathbf{u}_L^{(i)}, p_L^{(i)})$, the resulting stress $\mathbf{f}_L^{(i)} = \pm\boldsymbol{\sigma}_L^{(i)} \cdot \mathbf{n}$ on the particle surface and the coefficients:

$$A_L^{(i,j)} = -\int_S \mathbf{e}_j \cdot \mathbf{f}_L^{(i)}\, dS\,, \tag{5a}$$

$$B_L^{(i,j)} = -\int_S [\mathbf{r} \wedge \mathbf{f}_L^{(i)}] \cdot \mathbf{e}_j\, dS. \tag{5b}$$

Note that from the dimensions Pa.s/m of $\mathbf{f}_T^{(i)}$ and Pa.s of $\mathbf{f}_R^{(i)}$, the dimension of A_T is N.m^{-1}s, that of A_R and B_T is N.s and that of B_R is N.m.s.

From Lorentz reciprocal theorem (Lorentz (1897), as detailed e.g. in Happel and Brenner (1991)):

$$\int_{S\cup\Sigma} \mathbf{u} \cdot \mathbf{f}_L^{(i)}\, dS = \int_{S\cup\Sigma} \mathbf{u}_L^{(i)} \cdot\ \boldsymbol{\sigma} \cdot \mathbf{n}\, dS. \tag{6}$$

Since both $\mathbf{u}$ and $\mathbf{u}_L^{(i)}$ vanish on the cavity walls Σ, it follows that:

$$A_T^{(i,j)} = A_T^{(j,i)}, \quad B_R^{(i,j)} = B_R^{(j,i)}, \quad A_R^{(j,i)} = B_T^{(j,i)}. \tag{7}$$

Adopting henceforth the usual tensor summation convention and setting $U_j = \mathbf{U} \cdot \mathbf{e}_j$ and $\Omega_j = \pm\Omega \cdot \mathbf{e}_j$, it follows (by linearity) that the flow field $(\mathbf{u}, p)$ applies on the particle the force $\mathbf{F}$ and torque $\mathbf{T}$ given from (3) by

$$\mathbf{F} = -[A_T^{i,j} U_j + B_T^{i,j} \Omega_j]\, \mathbf{e}_i\,, \tag{8a}$$

$$\mathbf{T} = -[A_R^{i,j} U_j + B_R^{i,j} \Omega_j]\, \mathbf{e}_i\,. \tag{8b}$$

From these expressions and the definitions (5), calculating $\mathbf{F}$ and $\mathbf{T}$ amounts to determine the stresses $\mathbf{f}_T^{(i)}$ and $\mathbf{f}_R^{(i)}$ induced on the particle surface S by these auxiliary flows. This is the so-called resistance matrix problem and the result is the grand resistance matrix constructed with the A_T, A_R, B_T, B_R matrices (with Cartesian components defined in (5)). The method to calculate the stresses $\mathbf{f}_T^{(i)}$ and $\mathbf{f}_R^{(i)}$ will be presented below in §2.2.

2.1.2 Case 2: Settling motion of a particle

For this case the particle and fluid are embedded in an uniform gravity field $\mathbf{g}$ and the particle settles as a rigid body with presently unknown velocities $(\mathbf{U}_s, \pm\Omega_s)$. For simplicity, particle inertia is neglected here. This assumption obviously applies

when the particle motion is steady. It is also appropriate to the unsteady (i.e. starting) motion of a solid particle in a liquid, since with densities of the same order it is consistent to neglect particle inertia when neglecting fluid inertia. The translational and rotational velocities $(\mathbf{U}_s, \pm\Omega_s)$ are then obtained from the particle equations of motion by requiring zero net force on and torque about the particle. Using (8) and assuming a solid particle with uniform density ρ_s then yields the following 6-equation linear system for the Cartesian velocity components:

$$A_T^{i,j}[\mathbf{U}_s \cdot \mathbf{e}_j] + B_T^{i,j}[\pm\Omega_s \cdot \mathbf{e}_j] = (\rho - \rho_s)\mathscr{V}\mathbf{g} \cdot \mathbf{e}_i, \tag{9a}$$

$$A_R^{i,j}[\mathbf{U}_s \cdot \mathbf{e}_j] + B_R^{i,j}[\pm\Omega_s \cdot \mathbf{e}_j] = 0. \tag{9b}$$

Since the left-hand-sides of (9) correspond to dissipative forces and torques, it is shown (see e.g. Kim and Karrila (1991)) that this system has a real-valued matrix which is not only symmetric (7) but also positive-definite. Accordingly, (9) admits a unique solution $(\mathbf{U}_s, \pm\Omega_s)$ which is obtained by first calculating on the particle's boundary the stresses $\mathbf{f}_T^{(i)}$ and $\mathbf{f}_R^{(i)}$ (i.e by first solving the previously-introduced Case 1).

2.2 Boundary integral formulation

This subsection shows how to obtain the surface stresses $\mathbf{f}_T^{(i)}$ and $\mathbf{f}_R^{(i)}$ for any arbitrarily-shaped solid particle and motionless closed cavity surface Σ. The starting point is the well-known integral representation of the Stokes velocity field in the entire fluid domain. The Cartesian components $G_{kj}(\mathbf{x},\mathbf{y})$ of the Oseen-Burgers tensor $\mathbf{G}(\mathbf{x},\mathbf{y})$ due to a point force located at the pole $\mathbf{y}$ are given by:

$$8\pi\mu G_{kj}(\mathbf{x},\mathbf{y}) = \frac{\delta_{kj}}{|\mathbf{x}-\mathbf{y}|} + \frac{[(\mathbf{x}-\mathbf{y})\cdot\mathbf{e}_k][(\mathbf{x}-\mathbf{y})\cdot\mathbf{e}_j]}{|\mathbf{x}-\mathbf{y}|^3} \tag{10}$$

(for j and $k = 1,2,3$) with δ_{kj} the kronecker delta. Following Youngren and Acrivos (1975, 1976) and Pozrikidis (1992), the integral representation for the fluid velocity at a point $\mathbf{x}$ in the fluid domain $\mathscr{D}$ is:

$$u_j(\mathbf{x}) = [\mathbf{u}\cdot\mathbf{e}_j](\mathbf{x}) = -\int_{S\cup\Sigma} [\mathbf{f}\cdot\mathbf{e}_k](\mathbf{y}) G_{kj}(\mathbf{x},\mathbf{y}) dS(\mathbf{y}), \tag{11}$$

where $\mathbf{f} = \pm\sigma\cdot\mathbf{n}$ is the stress exerted by the Stokes flow $(\mathbf{u}, p)$ governed by (1)-(2) on the entire surface $S\cup\Sigma$. The relationship (11) shows that the fluid velocity $\mathbf{u}$ is induced by a single-layer distribution of stresses $\mathbf{f}$ on both the particle S and cavity Σ surfaces. In general, the integral representation of a Stokes flow field involves two contributions: a single layer one as in (11) and a double-layer one. That one vanishes here (see Pozrikidis (1992)) because $\mathbf{u}$ is a rigid-body motion

on each surface S and Σ. Clearly, one can compute $\mathbf{u}$ in the entire fluid domain $\mathscr{D}$ with Eq. (11), once $\mathbf{f}$ is known on $S \cup \Sigma$. This required stress $\mathbf{f}$ is obtained by letting $\mathbf{x}$ tend onto the surface S in (11). Since each component $G_{kj}(\mathbf{x},\mathbf{y})$ is only weakly singular as $\mathbf{x}$ approaches $\mathbf{y}$ on S, it turns out that (11) remains valid for $\mathbf{x}$ on the particle surface S. Accordingly, the unknown stress is obtained from the various $\mathbf{f}_L^{(i)}$, solutions of the following Fredholm boundary-integral equation of the first kind:

$$[\mathbf{u}_L^{(i)} \cdot \mathbf{e}_j](\mathbf{x}) = -\int_{S\cup\Sigma} [\mathbf{f}_L^{(i)} \cdot \mathbf{e}_k](\mathbf{y}) G_{kj}(\mathbf{x},\mathbf{y}) dS(\mathbf{y}) \text{for } \mathbf{x} \text{ on } S \cup \Sigma\,, \tag{12}$$

with $\mathbf{u}_L^{(i)}$ prescribed on S and Σ as in (4). As previously noticed, the pressure field p of the solution $(\mathbf{u}, p)$ to (1)-(2) is defined up to a constant. Therefore, the local stress $\mathbf{f} = \boldsymbol{\sigma} \cdot \mathbf{n}$ on S is defined up to a vector that is a multiple of the unit normal $\mathbf{n}$. That is, this property when written in (12) is the identity

$$\left\{ \int_{S\cup\Sigma} [\mathbf{n} \cdot \mathbf{e}_k](\mathbf{y}) G_{kj}(\mathbf{x},\mathbf{y}) dS(\mathbf{y}) \right\} \cdot \mathbf{e}_j = 0 \tag{13}$$

which holds for $\mathbf{x}$ located on $S \cup \Sigma$ and also for $\mathbf{x} \to \infty$ (see Pozrikidis (1992)). In summary, the boundary-integral equation (12) provides the stress $\mathbf{f} = \pm\boldsymbol{\sigma} \cdot \mathbf{n}$ on the entire surface $S \cup \Sigma$. It does not admit a unique solution since $\mathbf{f}$ is obtained on $S \cup \Sigma$ up to $\lambda\mathbf{n}$ with λ constant. It should be remarked that adding $\lambda\mathbf{n}$ to $\mathbf{f}$ in (3), (5) and (11) does not affect the results, in particular the solutions to Cases 1 and 2 .

2.3 Basic Remarks

The approach presented in §2.1 and §2.2 is valid in essence for any arbitrarily-shaped particle S and cavity Σ surfaces. As to the practical application, a few basic remarks are appropriate.

(i) When discretized, equation (12) still admits a non-singular influence matrix and therefore a unique solution $\mathbf{f}$ which, not surprisingly, depends on the selected mesh on $S \cup \Sigma$ (more precisely, the differences between the exact solution $\mathbf{f}$ and computed solution $\mathbf{f}'$ takes the form $\lambda\mathbf{n}$ with λ constant on $S \cup \Sigma$).

(ii) The proposed boundary integral equation (12) involves the stress $\mathbf{f}$ on the *entire* surface $S \cup \Sigma$. As discussed in the introduction, it is sometimes possible to use instead of the Oseen-Burgers Green tensor $\mathbf{G}$ defined by (10) another Green tensor $\mathbf{G}^c$ which vanishes on the cavity, i.e such that its Cartesian components $G_{ij}^c(\mathbf{x},\mathbf{y})$ vanish for $\mathbf{x}$ on Σ. In such a case, the result is a boundary-integral equation obtained by replacing in (12) $S \cup \Sigma$ and $G_{kj}(\mathbf{x},\mathbf{y})$ with S and $G_{kj}^c(\mathbf{x},\mathbf{y})$, respectively. The main advantage is that the only stress $\mathbf{f}$ to be determined is that on the particle surface S and therefore only this surface has to be meshed (i.e there is no need to mesh the

cavity). Such an efficient approach was previously worked out in Sellier (2008) for a *spherical* cavity. This type of approach is based on the availability of the "cavity Green tensor" G^c which is, up to now, known analytically only for very particular geometries. Now, this Green tensor might be in principle calculated numerically. However, this strategy would be much more CPU time consuming than directly solving the boundary-integral equation (12) for the usual Oseen Burgers tensor G. Therefore, the present work is based on a direct solution of (12) for which it proposes a relevant numerical strategy, that is efficient even for large cavities.

3 Numerical implementation and benchmarks

This section presents the proposed numerical implementation for inverting the boundary-integral equation (12) in the case of a rectangular cavity. It also performs benchmark tests by comparing to accurate earlier results for a fluid confined between two parallel or perpendicular plane walls (see Bhattacharya, Bławzdziewicz, and Wajnryb (2005), Sano and Hasimoto (1976)) and with computations achieved with the finite elements commercial software Comsol for a rectangular cavity.

3.1 The boundary element technique

For details about the boundary element technique, the reader is refered to classical textbooks (C. A. Brebbia and Wrobel (1984), Domingez (1993), Beskos (1998), Bonnet (1999)) and also to papers by Pasol and Sellier (2006) and Sellier (2007). Each curvilinear triangular boundary element Δ_e is mapped onto the standard triangle Δ with inequations $0 \leq \xi_1 \leq 1$, $0 \leq \xi_2 \leq 1$, $\xi_1 + \xi_2 \leq 1$. The location $\mathbf{y}$ and the unknown stress $\mathbf{f}(\mathbf{y})$ on this 6-node isoparametric boundary element Δ_e are expanded as:

$$\mathbf{y} = \sum_{q=1}^{6} M_q(\xi)\mathbf{y}_q^e, \qquad \mathbf{f}(\mathbf{y}) = \sum_{q=1}^{6} M_q(\xi)\mathbf{f}(\mathbf{y}_q^e), \tag{14}$$

where $\mathbf{y}_q^e$ are the nodal points belonging to the element Δ_e and $M_q(\xi)$ is a quadratic interpolation function with $\xi = (\xi_1, \xi_2)$ located on Δ. In discretizing the boundary-integral equation (12) at the node $\mathbf{x}$ on $S \cup \Sigma$, the following integrals have to be computed accurately:

$$I_{kj}^{e,q}(\mathbf{x}) = \int_{\Delta} G_{kj}(\mathbf{x}, \mathbf{y})[M_q J](\xi) d\xi_1 d\xi_2, \tag{15}$$

in which J is the Jacobian of the mapping from Cartesian cordinates $\mathbf{y}_i(\xi) = \mathbf{y}(\xi) \cdot \mathbf{e}_i$ to intrinsic coordinates ξ_1, ξ_2. In adequately handling the integral $I_{kj}^{e,q}(\mathbf{x})$, two alternative circumstances occur:

(i) Either the point $\mathbf{x}$ does not belong to the boundary element Δ_e. Since it is regular, the integral is then evaluated with standard Gaussian quadratures (see e.g. Lyness and Jespersen (1975); Stroud and Secrest (1966)).
(ii) Or the point $\mathbf{x}$ is one node of Δ_e. In that case $G_{kj}(\mathbf{x},\mathbf{y})$ becomes weakly singular as $\mathbf{y}$ tends to $\mathbf{x}$ on Δ_e. The weak singularity at $\mathbf{x}$ is removed by using polar coordinates on the pattern Δ, as detailed in Bonnet (1999). It should be remarked that in both cases (i) and (ii) a regular integral on Δ is evaluated using Gaussian quadratures of either low, medium, or high order, depending upon the location of $\mathbf{x}$ with respect to the element Δ_e.The way to select the proper order of quadrature in order to ascertain a given accuracy is a key issue which has not yet received a mathematical background. For the present work, we adopted the well tested proposition of H. Rezayat and Rizzo (1986). Once discretized by distributing N nodal points on $S \cup \Sigma$, the integral equation(12) takes the form of a linear system $AX = B$ with a fully-populated and non symmetric $3N \times 3N$ influence matrix A. This system is then inverted by Gaussian elimination.

3.2 Adaptative mesh refinement

In practice, the cavity Σ might be large as compared with the typical particle dimension. It is then more efficient to adapt a non-uniform mesh on Σ, that is boundary elements Δ_e with different sizes depending upon the location of the particle. Accordingly, for a small particle-cavity gap it is necessary to distribute enough nodal points on Σ near the particle and less nodal points elsewhere on Σ. The choice of an adequate non-uniform mesh is a key issue in order to achieve a good accuracy of the boundary element approach at a reasonable CPU time and RAM memory cost. For a particle with length scale a and a particle-cavity gap of order η (here η denotes the smallest distance from a point of the particle surface to Σ), we obtain a suitable mesh of $S \cup \Sigma$ by proceeding as follows:
(i) Step 1 : First, the particle is meshed using 6-node curvilinear triangular boundary elements with typical size of the order of the particle-cavity gap η or less.
(ii) Step 2 : An initial rough mesh is constructed on Σ by using 6-node flat (for a rectangular cavity) triangular boundary elements Δ_e^r.
(iii) Step 3 : Finally, one iteratively refines each element Δ_e^r depending on its distance η_e to the particle and its typical length δ_e. The refinement consists in dividing the triangle Δ_e^r in four sub-triangles if $\delta_e > \eta_e$. This last step is repeated as many times as necessary for a prescribed accuracy to be achieved. The cases of a sphere located near two walls or three walls of a cubic cavity and at the center of a cubic cavity are illustrated in Figure 2 and 3, respectively.

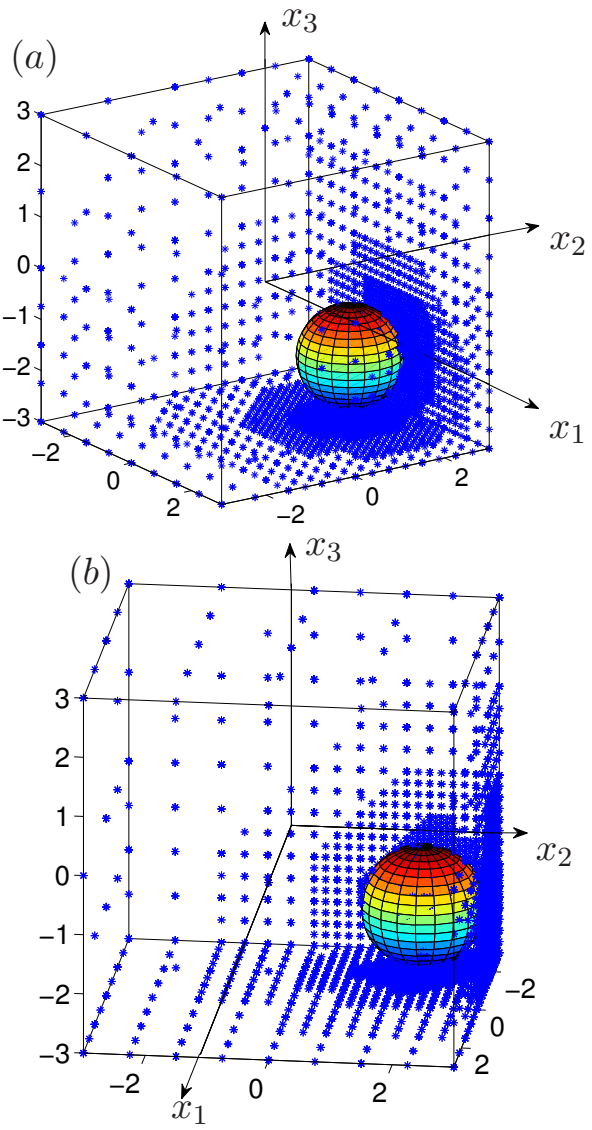

Figure 2: Adaptative mesh on a cubic cavity ($L_1 = L_2 = L_3 = 6a$) for a spherical particle with radius a and center O_1 close to either two or three walls: (a) case of two close walls with $O_1 = (0, 1.9a, -1.8a)$; (b) case of three close walls with $O_1 = (-1.9a, 1.9a, -1.9a)$.

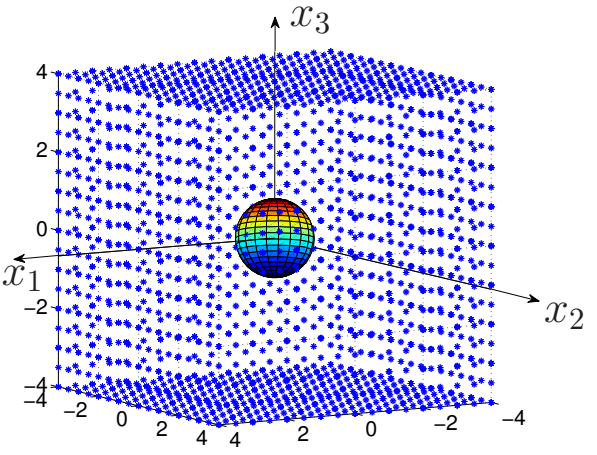

(b)

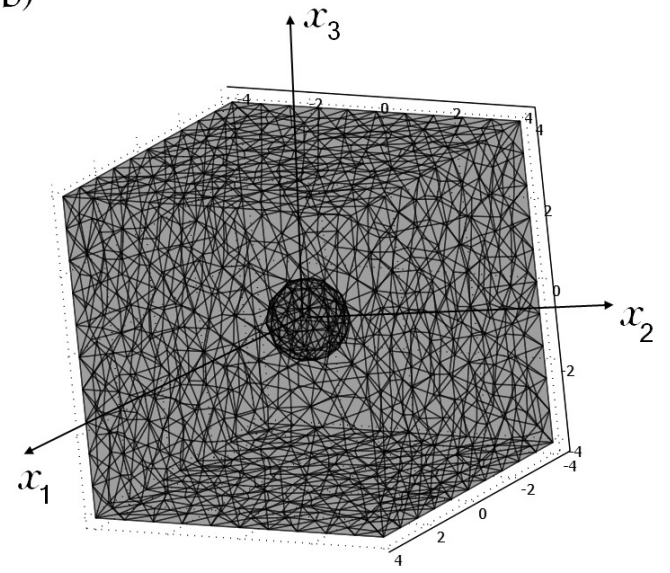

Figure 3: Sphere with radius a at the center of a cubic cavity with size $4a$. (a) Meshes for the present Boundary Element Method (putting $N_s = 1058$ and $N_c = 1538$ nodal points on the sphere and cavity respectively). (b) External view of the 15615 three-dimensional finite elements used with the Comsol FEM software.

3.3 Numerical benchmarks

This subsection presents results and comparisons for a spherical particle with radius a and a rectangular cavity. Such circumstances are depicted in Figure 1. First, the sphere is located at the center of a cubic cavity with sides $L_1 = L_2 = L_3 = 2h$. The sphere translates at a prescribed velocity $\mathbf{U}$ without rotation ($\pm\Omega = \mathbf{0}$). Because of its symmetric location, it experiences no torque and a drag force $\mathbf{F}$ directed along its velocity with

$$\mathbf{F} = -6\pi\mu a\lambda\mathbf{U}, \qquad \lambda = \lambda(h/a), \tag{16}$$

where $\lambda > 0$ is a normalized friction coefficient which tends to unity as h/a becomes large. Note that, by matching with (8a), the following relationship holds: $6\pi\mu a\lambda = A_T^{(1,1)} = A_T^{(2,2)} = A_T^{(3,3)}$. The computed values of λ are displayed versus h/a in Table 1 and plotted in Figure 4. It is found that, in order to keep the shown accuracy, the number N_s of nodal points on the sphere may be kept constant whereas the number N_c of nodal points on the cavity should be increased for small gap. The results are compared to ones obtained with the Comsol finite elements software.

Table 1: Results for the friction factor λ on a sphere located at the center of a cubic cavity versus the normalized half-side of the cavity, from the boundary element method (BEM) and the Comsol package (C). N_s and N_c denote the number of nodal points used in BEM on the sphere and cavity, respectively.

h/a	$\lambda(BEM)$	$\lambda(C)$	N_s	N_c
1.1	72.51	79.96	1058	2702
1.5	11.41	11.64	1058	2702
1.9	5.377	5.412	1058	1790
2.044	4.535	4.541	1058	1538
3	2.433	2.425	1058	1538
4	1.851	1.847	1058	1538
6	1.462	1.462	1058	1538
8	1.315	1.313	1058	1538
10	1.238	1.237	1058	1538
14	1.160	1.162	1058	1538
21.5	1.099	1.090	1058	1538
35	1.059	1.056	1058	1538
55	1.018	1.035	1058	1538

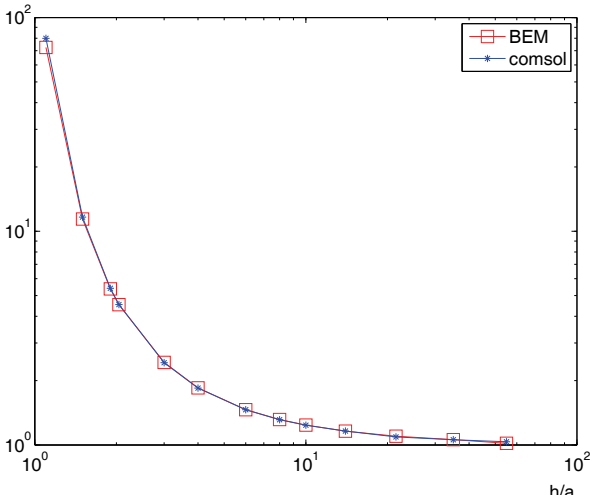

Figure 4: Plot of λ versus h/a. Results using the BEM approach ($\square$) and the Comsol package ($\star$).

The meshes used in our method and in our Comsol finite elements calculation for $h = 4a$ are shown in Figure 3(a) and 3(b) respectively. Table 1 shows that a good agreement between $\lambda(BEM)$ and $\lambda(C)$ is obtained within a $O(10^{-2})$ accuracy, which is typical of the Comsol software for a fully three-dimensional Stokes flow. This accuracy of Comsol is also illustrated in Table 2 for a sphere located at the center of a spherical cavity.

β	1.1	2	5
λ	1623.9	7.2797	1.7151
λ_t	1624.0	7.2941	1.7558
$\Delta = \lvert\lambda/\lambda_t - 1\rvert$	0.0001	0.0020	0.0232

Table 2: Friction coefficient for a sphere with radius a located at the center of a spherical cavity with radius βa: computed results λ using the Comsol FEM software, analytical results λ_t calculated by Eq. (22) and relative difference Δ.

A second comparison is shown for a sphere located at the center of a non-cubic rectangular cavity with $L = L_1 = L_2$ and $L_3 = 2H$ (Figure 1), still using a N_s-node and N_c-node mesh on the sphere and cavity, respectively. The sphere translates in a direction normal to $\mathbf{e}_2$ without rotating. The drag force $\mathbf{F}$, which is not in general

directed along **U**, may be written as

$$\mathbf{F} = -6\pi\mu a[\lambda_1 U_1 \mathbf{e}_1 + \lambda_3 U_3 \mathbf{e}_3] \tag{17}$$

and the torque **T** vanishes by symmetry. A partial comparison is possible here with results obtained by Bhattacharya, Bławzdziewicz, and Wajnryb (2005) for an open fluid domain bounded by two stationary *parallel* plane walls. That case is incorported here by considering the walls located at $x_3 = 0$ and $x_3 = 2H$, as depicted in Figure 5, and letting $L \to \infty$.

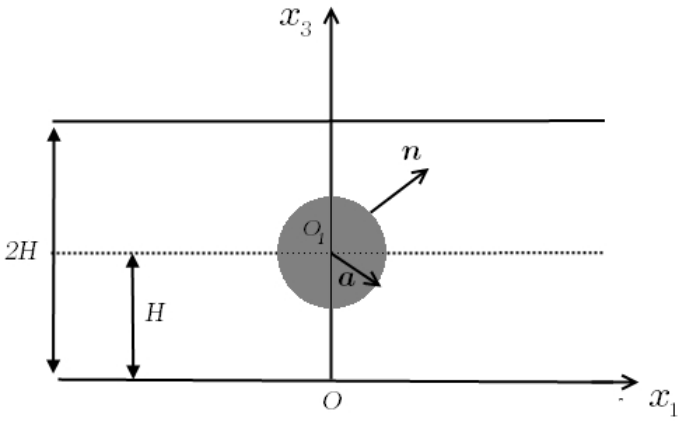

Figure 5: Notation for a spherical particle immersed in a fluid bounded by the $x_3 = 0$ and $x_3 = 2H$ planes.

Bhattacharya, Bławzdziewicz, and Wajnryb (2005) used the hydromultipole technique which provide accurate results. Their data may be represented also as in (17), with normalized friction coefficients λ_1^B and λ_3^B. Our results for λ_1, λ_3 for $L/a = 10, 30, 50$ are compared to their values λ_1^B, λ_3^B for $L \to \infty$ in Table 3 for three values of H/a. It is observed that the relative difference $\Delta_{\lambda_i} = |\lambda_i/\lambda_i^B - 1|$ (for $i = 1$ and 3) decays when increasing the number of nodes N_s and N_c distributed on the sphere S and cavity Σ, respectively.

Our last comparisons concern a sphere with radius a immersed in a fluid bounded by two *perpendicular* plane solid walls. These circumstances are depicted in Figure 6 and the force **F** exerted on the sphere translating with the velocity **U** has the

N_s	N_c	L/a	H/a	λ_1, λ_1^B	$\Delta\lambda_1$	λ_3, λ_3^B	$\Delta\lambda_3$
74	3940	10	1.209	3.181	0.0049	9.948	0.047
242	3998	10	1.209	3.200	0.0012	10.31	0.013
B		∞	1.209	3.196		10.44	
74	822	30	2.862	1.485	0.0112	1.883	0.013
242	822	30	2.862	1.482	0.0081	1.889	0.010
B		∞	2.862	1.502		1.908	
74	590	50	11	1.100	0.0002	1.148	0.034
242	590	50	11	1.103	0.0025	1.150	0.001
B		∞	11	1.100		1.151	

Table 3: Drag coefficients of a sphere in a rectangular cavity. N_s and N_c are the numbers of nodes on the sphere and cavity, respectively. Comparison of our results λ_1, λ_3 in the cases $L/a = 10, 30, 50$ to the results (denoted with B) λ_1^B, λ_3^B of [4] in the case of two parallel planes ($L \to \infty$). The relative differences $\Delta\lambda_i = |\lambda_i/\lambda_i^B - 1|$ (for $i = 1$ and 3) are also shown.

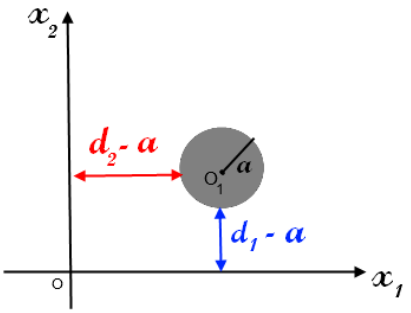

Figure 6: A sphere in a fluid bounded by two *perpendicular* plane walls at $x_1 = 0$ and $x_2 = 0$.

following components:

$$\mathbf{F} = -6\pi\mu a U(F_1\mathbf{e}_1 + F_2\mathbf{e}_2) \quad \text{if} \quad \mathbf{U} = U\mathbf{e}_1, \tag{18}$$

$$\mathbf{F} = -6\pi\mu a U F_3\mathbf{e}_3 \quad \text{if} \quad \mathbf{U} = U\mathbf{e}_3, \tag{19}$$

with friction coefficients F_i depending upon the sphere to wall gaps $d_1 - a$ and $d_2 - a$. For a sufficiently distant sphere with $\varepsilon = a/\min(d_1, d_2) \ll 1$, Sano and Hasi-

moto (1976) obtained asymptotic expansions of coefficients F_i at order ε. These approximations are compared in Table 4 in the case $\varepsilon = 0.1$ to our numerical results obtained for large values of L_1, L_2 and L_3 (We chose values of $L/a = L_1/a = L_2/a = L_3/a$, as shown in Table 4).

d_1/d_2	F_1	F_1 (Sano)	F_2	F_2 (Sano)	F_3	F_3 (Sano)	L/a
1	1.144	1.126	0.013	0.010	1.089	1.082	400
1.6	1.099	1.090	0.072	0.006	1.072	1.067	500
2	1.085	1.079	0.004	0.004	1.067	1.063	600

Table 4: Friction coefficients F_i for a sphere near two perpendicular walls in the case $\varepsilon = 0.1$ and comparison with Sano & Hasimoto [42] approximation at order ε.

As observed in Table 4, our results are in good agreement with the asymptotic formulae of Sano and Hasimoto (1976): that is, the difference is consistent with the neglected $O(\varepsilon^2)$ terms in their approach.

4 Numerical results

This section presents and discusses numerical results both for spherical and ellipsoidal particles.

4.1 Case of a solid spherical particle

4.1.1 Prescribed rigid-body motion

We consider a sphere with radius a and center O_1 and two alternative cavities with center O: a cubic one with side length $2h > 2a$ and a spherical one with radius $R > a$. In view of a comparison, we choose R so that the volume of cavities is the same:

$$R = \left(\frac{6}{\pi}\right)^{1/3} h. \tag{20}$$

The sphere is located in one plane of symmetry of the cavity with either $O_1 = O$ (sphere centered at the cavity center) or $O_1 \neq O$. The relevant notation is depicted in Figure 7.

By symmetry, when the sphere with imposed translational and angular velocities $\mathbf{U}$ and $\pm\Omega$ is located at the cavity center, it experiences the following force $\mathbf{F}$ and torque $\mathbf{T}$ (with respect to its center O_1):

$$\mathbf{F} = -6\pi\mu a\lambda_t \mathbf{U}, \quad \mathbf{T} = -8\pi\mu a^3 \lambda_r \pm \Omega\,. \tag{21}$$

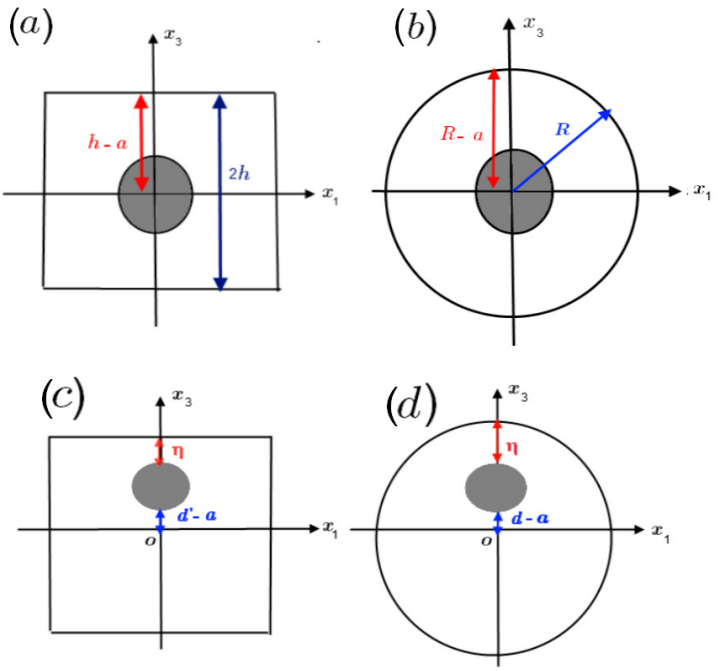

Figure 7: A sphere located either at the center (cases (*a*) and (*b*)) or in a plane of symmetry (cases (*c*) and (*d*)) of two volume- equivalent cubic and spherical cavities.

The friction coefficients λ_t and λ_r for the force $\mathbf{F}$ and torque $\mathbf{T}$ (about the sphere center), respectively, depend upon the cavity shape and size. When the sphere is located at the center of the spherical cavity, analytical results are available (see e.g. Happel and Brenner (1991)) for both λ_t and λ_r:

$$\lambda_t = \frac{1-\beta^5}{1-\frac{9}{4}\beta+\frac{5}{2}\beta^3-\frac{9}{4}\beta^5+\beta^6}, \tag{22}$$

$$\lambda_r = \frac{1}{1-\beta^3} \text{ for } \beta = \frac{a}{R} < 1. \tag{23}$$

In contrast, for the cubic cavity an analytical result (e.g. using the method of reflexions) would be difficult to obtain. Thus a simpler evaluation of the coefficients λ_t and λ_r requires numerics. Computed coefficients are plotted in Figure 8 versus the normalized size h/a of the cubic cavity (Eq. (20) then provides the radius of the spherical cavity).

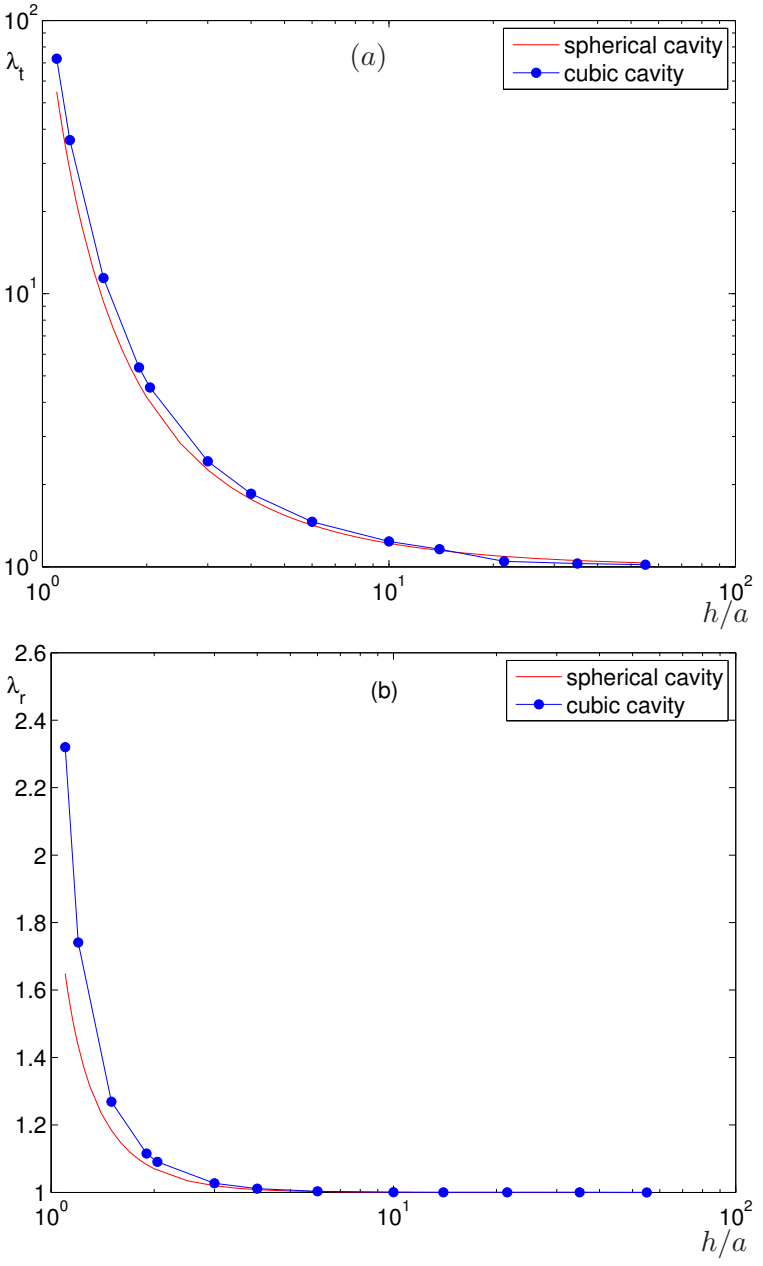

Figure 8: Friction coefficients for (a) translation (λ_t) and (b) rotation (λ_r) of a sphere centered in a spherical and a cubic cavity. The solid curves represent the analytical expressions (22)-(23) for the spherical cavity. The symbols (joined by lines as a guide to the eye) represent our computed results for the cubic cavity.

It turns out that both for a pure translation (λ_t) and a pure rotation (λ_r) the cubic cavity yields stronger wall-sphere interactions (higher values for the friction coefficient) than the spherical cavity. Although the sphere-cavity gap for the cubic cavity, $h-a$ is smaller than its value $R-a \sim 1.24h-a$ for the spherical cavity, it should be remarked that this minimum gap is actually reached on the entire sphere surface of the spherical cavity. Then this geometrical configuration results in larger friction coefficients. Note also that, for both cavities, sphere-cavity interactions decay much faster for λ_r than for λ_t as the cavity becomes large.

4.1.2 Settling motion of a spherical particle

Let us now examine the motion of a sphere with radius a and uniform density ρ_s settling in an uniform gravity field $\mathbf{g} = -g\mathbf{e}_3$ (see Figure 1). We consider a cubic cavity with mid-size $3a$, and locate the sphere center O_1 in the $x_2 - x_3$ plane, i.e select $\mathbf{OO_1}.\mathbf{e}_1 = 0$. Under these assumptions, the settling sphere translational and angular velocities $\mathbf{U}$ and $\pm\Omega$, obtained as explained in §2.1.2, read $\mathbf{U} = U_2\mathbf{e}_2 + U_3\mathbf{e}_3$ and $\pm\Omega = \Omega_1\mathbf{e}_1$. Setting $\mathbf{OO_1} = d_2\mathbf{e_2} + d_3\mathbf{e_3}$, symmetries make it further possible to restrict the attention to the values $0 \leq d_2 < 2a$ and $-2a < d_3 \leq 0$. Non-zero velocity components may then be normalized as follows:

$$u_2 = \frac{9\mu\, U_2}{2g(\rho-\rho_s)a^2}, u_3 = \frac{9\mu\, U_3}{2g(\rho-\rho_s)a^2}, \tag{24}$$

$$\omega_1 = \frac{9\mu\, \Omega_1}{2g(\rho-\rho_s)a} \tag{25}$$

They are based on the Stokes settling velocity $2(\rho_s-\rho)a^2\mathbf{g}/(9\mu)$ of the sphere when immersed in an unbounded fluid. Results for u_2, u_3, ω_1 versus $0 \leq d_2 \leq 1.9a$ for $d_3/a = 0, -1, -1.5, -1.8$ are displayed in Figure 9.

The u_2 component vanishes for $d_3 = 0$ by symmetry and is thus not shown in Figure 9 (a). Note that u_3 decreases strongly for a given value of d_2 as d_3 increases in magnitude (i.e as the sphere approaches the cavity bottom). In contrast, u_2 is less affected as d_3 and d_2 change. Actually, sphere-cavity interactions are larger for the velocity component normal to a close boundary for (u_3) than for the velocity component (u_2) tangent to it. In all cases, the sphere angular velocity ω_1 is low. For symmetry reasons, $\omega_1 = 0$ for $d_2 = 0$ for any value of d_3. Furthermore, $\omega_1 > 0$ for any $d_2 > 0$ when the sphere is not close to the $x_3 = -3a$ bottom side of the cavity. In contrast, for $d_3 = -1.8a$ (close to the bottom side), ω_1 is either positive or negative, depending upon d_2, and vanishes at $d_2 \sim 1.3a$. Of course, larger particle-wall interactions are expected when the sphere lies close to three walls, as sketched

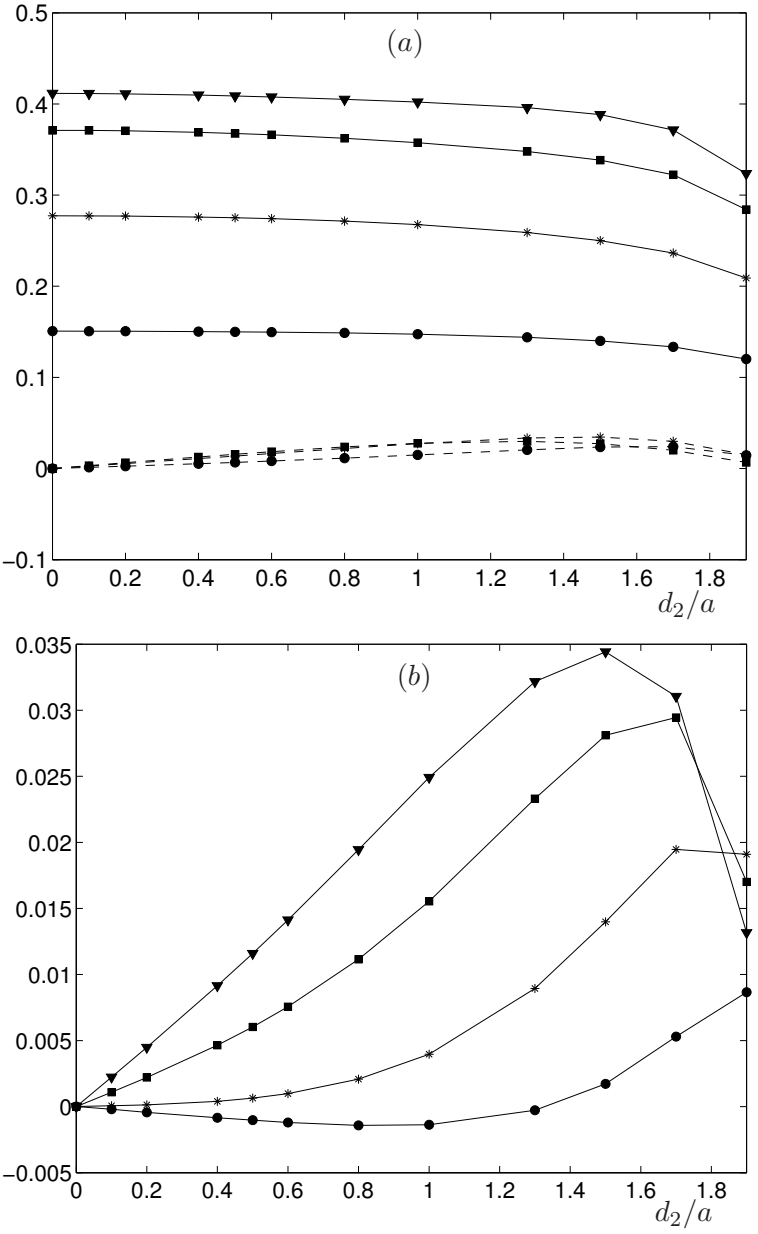

Figure 9: Normalized settling translational and angular velocities versus $0 \leq d_2 < 1.9a$ for $d_3/a = 0(\blacktriangledown)$, $d_3/a = -1(\blacksquare)$, $d_3/a = -1.5(\star)$, $d_3/a = -1.8(\bullet)$ for a cubic cavity with mid-size $3a$. (*a*) Translational velocities u_3 (solid lines) and u_2 (dashed lines). (*b*) Angular velocities ω_1.

in Figure 2(b). We thus also look at the settling rigid-body migration of the sphere (again for $\mathbf{g} = -g\mathbf{e}_3$ and the cubic cavity with center O and mid-size $3a$) with center O_1 such that $\mathbf{OO_1} = (d-2a)(\mathbf{e}_1 - \mathbf{e}_2 + \mathbf{e}_3)$ for $0 < d \ll 2a$. In that case, it is easily shown by symmetry that $\mathbf{U} = U_2(\mathbf{e}_2 - \mathbf{e}_1) + U_3\mathbf{e}_3$ and $\pm\Omega = \Omega_1(\mathbf{e}_1 + \mathbf{e}_2)$. The associated normalized velocities u_2, u_3 and ω_1 (recall (24)-(25)) are plotted in Figure 10.

As d vanishes, the sphere approaches the cavity corner and hydrodynamic interactions with the three cavity walls then strongly increase the velocity component u_3 parallel to gravity. In contrast, other components $u_2 = -u_1$ and angular velocities $\omega_1 = \omega_2$ reach a maximum value (i.e. the largest boundary effects occur) for values of d/a of medium magnitude ($d/a \sim 0.6$ and $d/a \sim 0.8$, respectively).

4.2 Case of a solid ellipsoidal particle

Cavity-particle interactions are expected to depend upon the particle shape. To investigate this basic issue, we consider in this section a particle of ellipsoidal shape with center O_1 and semi-axes a_i in the $\mathbf{e}_i$ directions ($i = 1,2,3$). Hence, the ellipsoid and the rectangular cavity have parallel planes of symmetry. For a given cavity, it is practically significant to consider a given fluid volume, i.e to select ellipsoids having the same volume as a sphere with radius a. Therefore, we henceforth take $a_1a_2a_3 = a^3$. We choose for the numerical computations the values $a_1 = a$, $a_2 = 0.8a$ and $a_3 = (1/0.8)a$.

4.2.1 Prescribed rigid-body of the ellipsoid

The selected volume-equivalent ellipsoid is located at the center of a cubic cavity ($L = L_1 = L_2 = L_3$ and $O_1 = O$). From symmetries, it is then shown that for imposed translational and angular velocity $\mathbf{U}$ and $\pm\Omega$ the hydrodynamic force $\mathbf{F}$ and torque $\mathbf{T}$ (about O_1) exerted on the ellipsoid read:

$$\mathbf{F} = -6\pi\mu a \sum_{i=1}^{3} R_i \lambda_t^{(i)} (\mathbf{U}.\mathbf{e}_i)\mathbf{e}_i, \tag{26}$$

$$\mathbf{T} = -8\pi\mu a^3 \sum_{i=1}^{3} \Lambda_i \lambda_r^{(i)} (\pm\Omega.\mathbf{e}_i)\mathbf{e}_i. \tag{27}$$

When the cubic cavity becomes large ($L \gg a$), the friction coefficients $\lambda_t^{(i)}$ and $\lambda_r^{(i)}$ asymptote unity and the normalized force and torque coefficients are from Jeffery (1922) (see e.g. Happel and Brenner (1991)):

$$R_i = \frac{8a_1a_2a_3}{3a(\chi + \alpha_i a_i^2)}, \tag{28}$$

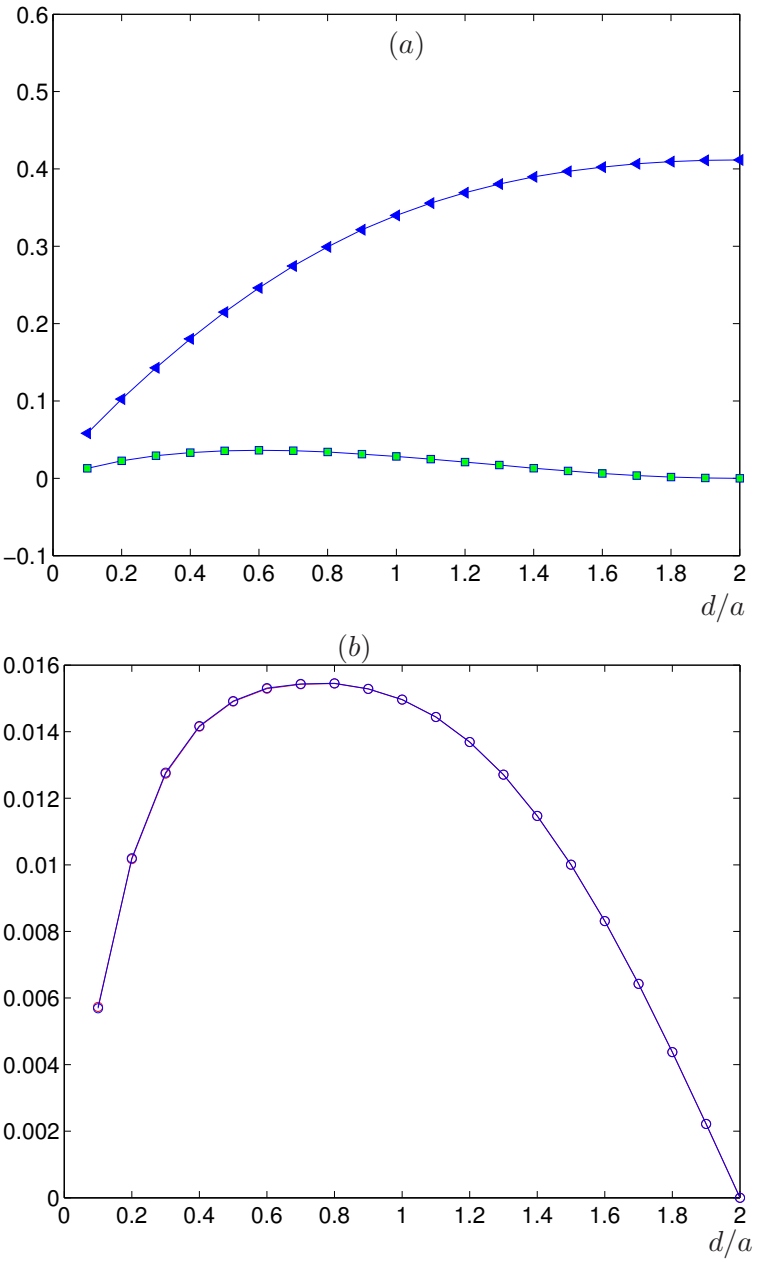

Figure 10: Normalized settling velocities for a sphere with center O_1 such that $\mathbf{OO_1} = (d-2a)(\mathbf{e}_1 - \mathbf{e}_2 + \mathbf{e}_3)$. (a) $u_2 = -u_1$ ($\square$) and u_3 ($\blacktriangleright$). (b) Angular velocities $\omega_1 = \omega_2$ ($\circ$).

$$\Lambda_i = \frac{2(a_1^2+a_2^2+a_1^3-a_i^2)}{3(a_1^2\alpha_1+a_2^2\alpha_2+a_3^2\alpha_3-a_i^2\alpha_i)}, \tag{29}$$

with:

$$\chi = a_1a_2a_3\int_0^\infty \frac{dt}{\Delta(t)}, \alpha_i = \int_0^\infty \frac{dt}{(a_i^2+t)\Delta(t)}, \tag{30}$$

$$\Delta(t) = \{(a_1^2+t)(a_2^2+t)(a_3^2+t)\}^{1/2}. \tag{31}$$

with $i = 1,2,3$ (Note that there is no summation over repeated indices i in (28)-(30)). The above coefficients R_i and Λ_i for the addressed ellipsoid $a_1 = a, a_2 = 0.8a, a_3 = (1/0.8)a$ have been calculated using the Maple Software. The results are: $R_1 \sim 0.970$, $R_2 \sim 1.060$, $R_3 \sim 1.014$, $\Lambda_1 = 22.930$, $\Lambda_2 = 30.006$ and $\Lambda_3 = 27.992$. The frictions coefficients $\lambda_t^{(i)}$ and $\lambda_r^{(i)}$ introduced by (26)-(27) were computed for different cubic cavities with mid-size $L/2$ and are plotted versus L/a in Figure 11.

The $\lambda_t^{(i)}$ and $\lambda_r^{(i)}$ coefficients directly measure to which extent the ellipsoid-cavity interactions affect the imposed translation or rotation parallel to the $\mathbf{e_i}$ direction when compared with the motion in unbounded fluid. The comparison of Figures 8 and 11 shows that these interactions may be either stronger or weaker than for the volume-equivalent sphere.

4.2.2 Settling ellipsoid

This last subsection examines the motion of the volume-equivalent ellipsoidal particle, with uniform density ρ_s, settling in a uniform gravity field aligned with one direction $\mathbf{e}_i$ $(i = 1,2,3)$. If immersed in an unbounded fluid with $\mathbf{g} \wedge \mathbf{e}_i = \mathbf{0}$, the ellipsoid is known to settle without rotation at the velocity (using Eq. (26) with $\lambda_t^{(i)} = 1$):

$$\mathbf{U}_i = \frac{2a^2(\rho_s-\rho)}{9\mu R_i}\mathbf{g} \text{ for } \mathbf{g} \wedge \mathbf{e}_i = \mathbf{0}. \tag{32}$$

When the fluid is confined by the cavity, the ellipsoid-cavity interactions affect the previous solution and also induce a possible rotation of the ellipsoid. These key effects are investigated for a cubic cavity with center O and mid size $2.5a$ when the ellipsoid representative equation is $x_1^2/a_1^2 + x_2^2/a_2^2 + x_3^2/a_3^2 = 1$ and its center O_1 is such that $\mathbf{OO_1} = d_2\mathbf{e}_2 + d_3\mathbf{e}_3$ with now $0 \le d_2 < 2.5a - a_2$ and $0 \le d_3 < 2.5a - a_3$. By superposition, we successively assume that $\mathbf{g}$ is parallel to $\mathbf{e}_1, \mathbf{e}_2$ and $\mathbf{e}_3$. The resulting normalized Cartesian velocity components are moreover defined as follows:

$$u_j = \frac{9\mu R_j \mathbf{U}.\mathbf{e}_j}{2a^2(\rho_s-\rho)g}, \omega_j = \frac{9\mu \pm \Omega.\mathbf{e}_j}{2a(\rho_s-\rho)g} \tag{33}$$

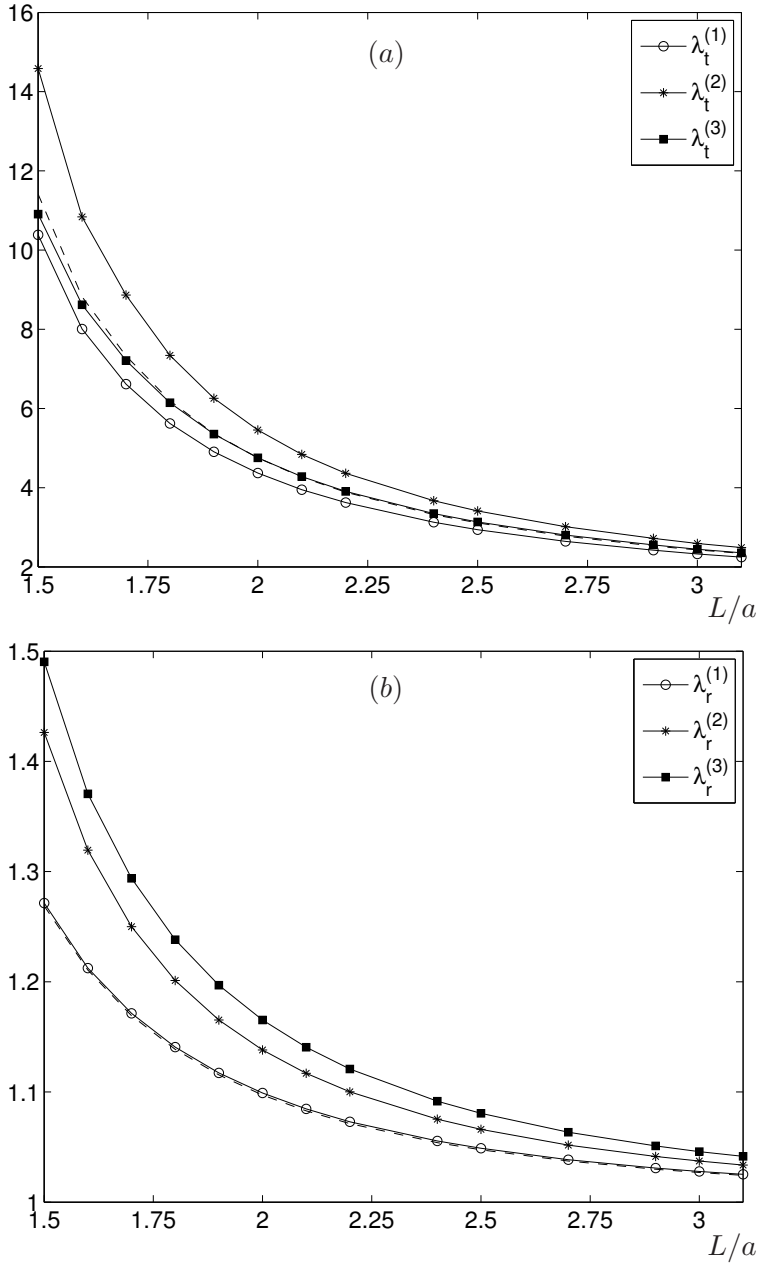

Figure 11: Results for the friction coefficients for an ellipsoid with dimensions $a_1 = 1, a_2 = 0.8a, a_3 = (1/0.8)\,a$ located at the center of a cubic cavity with side length L: (a) coefficients for translation, $\lambda_t^{(i)}$; (b) coefficients for rotation, $\lambda_r^{(i)}$. For comparison, the dashed lines show the values of λ_t and λ_r for a spherical particle with radius a.

(without summation over indices j) [1]. For our given cubic cavity and $\mathbf{OO_1}.\mathbf{e}_1 = 0$ the non-zero velocities u_j and ω_j depend upon the selected direction $\mathbf{e}_i$ of the gravity $\mathbf{g}$ and the data (d_2, d_3). These velocities, computed here for $d_3 = 0, 0.2, 0.8, 1.4$, are given for $\mathbf{g} \wedge \mathbf{e}_i = \mathbf{0}$ in Figure 12, 13 and 14 $(i = 1, 2, 3)$.

If $\mathbf{g} \wedge \mathbf{e}_1 = \mathbf{0}$ then, for symmetry reasons, $u_2 = u_3 = \omega_1 = 0$. The normalized velocity u_2 is at a maximum value ~ 0.36 for $d_2 = d_3 = 0$ (the ellipsoid being located at the cavity center) and decreases as d_2 or/and d_3 increases(s) with a lowest value ~ 0.24 for $d_2 = 1.6a$ and $d_3 = 1.4a$. Thus, the ellipsoid-cavity interactions for $\mathbf{g} \wedge \mathbf{e}_1 = \mathbf{0}$ can result in a 30% relative loss in settling velocity. Note that ω_2 is weakly sensitive to d_2 and strongly sensitive to d_3. The quantity ω_3 follows opposite behaviors. The ellipsoid settling velocity might be strongly affected for $\mathbf{g}.\mathbf{e}_1 = 0$ as revealed by Figures 13-14. For instance, for $\mathbf{g} \wedge \mathbf{e}_2 = \mathbf{0}$ then $u_1 = \omega_2 = \omega_3 = 0$, u_3 is weak and u_2 deeply depends upon d_2 and the ellipsoid-wall interactions may even result in a $\sim 80\%$ relative velocity loss (for $d_2 = 1.6a$ and $d_3 = 1.4a$). In addition the (weak) angular velocity ω_1 may either be positive or negative. Similar trends are observed in Figure 14 for $\mathbf{g} \wedge \mathbf{e}_3 = \mathbf{0}$ with now $u_1 = \omega_2 = \omega_1 = 0$.

5 Conclusions

Particle-cavity interactions in the low-Reynolds-number approximation are calculated accurately by incorporating refinements in the Boundary Elements Method. The method amounts to solve six Fredholm boundary-integral equations of the first kind governing the surface stress on the motionless cavity and the moving solid particle, for the six elementary motions of translation and rotation of the particle. Then, the method solely requires to mesh the particle and cavity surfaces. The refinements consist in simultaneously:

1. using six-node curvilinear triangular boundary elements;
2. building up adequately and iteratively a non-uniform mesh of the cavity to account for the particle shape and its proximity.

The numerical implementation is achieved here for a rectangular cavity, These refinements provide a good accuracy at a reasonable CPU time cost as demonstrated by several benchmarks against results obtained by previous authors. New numerical results are given and discussed for spherical and volume-equivalent ellipsoidal particles, thereby illustrating the ability of the proposed technique to deal with various particles. Not surprisingly, particle-cavity interactions are found to deeply depend upon the particle shape, location and also upon the experienced force and torque components, settling velocity components and applied gravity field.

[1] Note that such definitions are opposite to the ones given in $(24) - (25)$ for which $\mathbf{g} = -\mathbf{g}.\mathbf{e_3}$

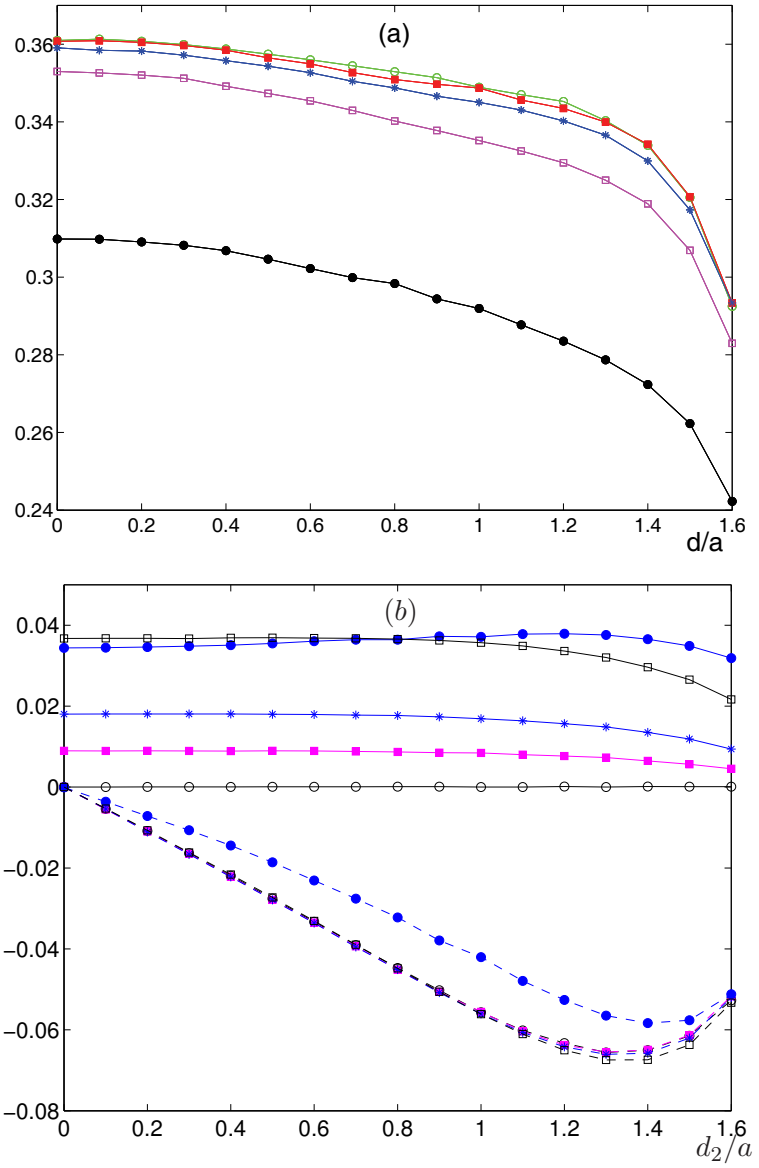

Figure 12: Non-zero normalized settling velocity components for $\mathbf{g} \wedge \mathbf{e}_1 = \mathbf{0}$ and $d_3/a = 0(\circ)$, $0.2(\blacksquare)$, $0.4(\star)$, $0.8(\square)$, $1.4(\bullet)$. (a) u_1. (b) ω_2 (solid lines) and ω_3 (dashed lines).

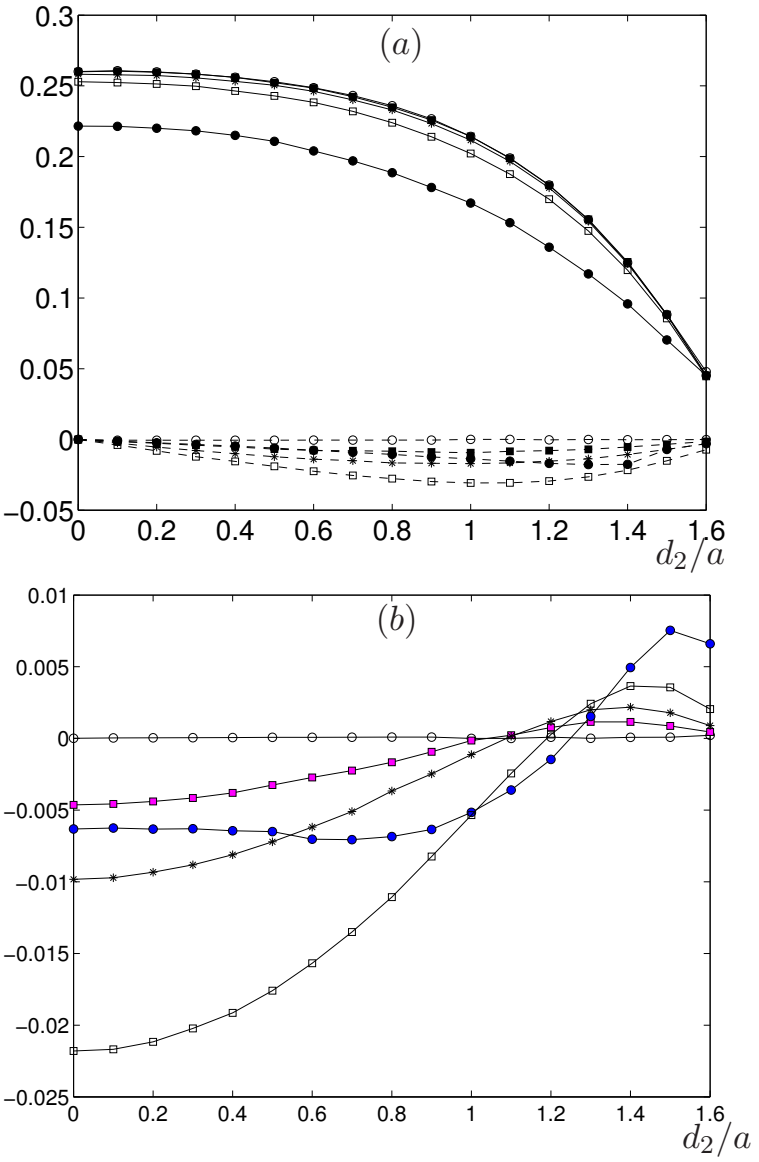

Figure 13: Non-zero normalized settling velocity components for $\mathbf{g} \wedge \mathbf{e}_2 = \mathbf{0}$ and $d_3/a = 0(\circ)$, $0.2(\blacksquare)$, $0.4(\star)$, $0.8(\square)$, $1.4(\bullet)$. (a) u_2 (solid lines) and u_3 (dashed lines). (b) ω_1.

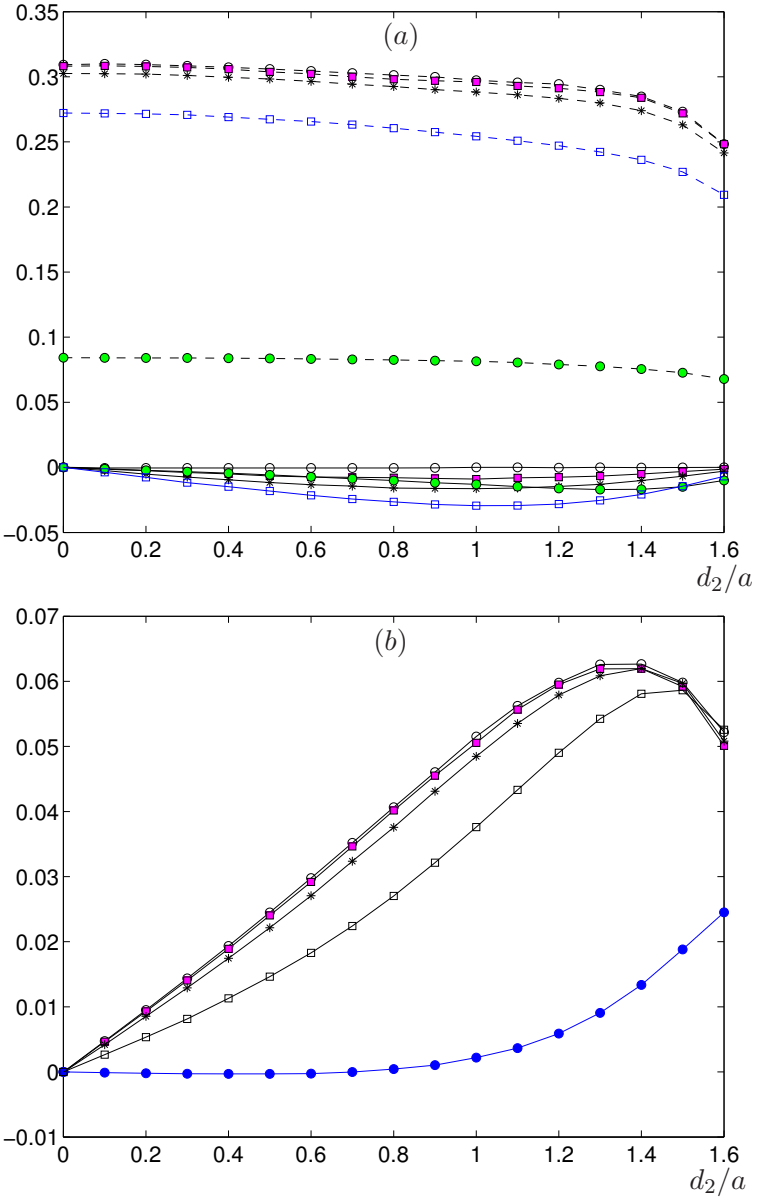

Figure 14: Non-zero normalized settling velocity components for $\mathbf{g} \wedge \mathbf{e}_3 = \mathbf{0}$ and $d_3/a = 0(\circ)$, $0.2(\blacksquare)$, $0.4(\star)$, $0.8(\square)$, $1.4(\bullet)$; (a): u_2 (Solid lines) and u_3 (dashed lines); (b): ω_1.

This approach may by essence adequately deal with arbitrarily-shaped cavity and particle. It should also be emphasized that the method may also efficiently cope with several interacting particles suspended in a fluid bounded by a cavity. Such a basic problem, in which both particle-particle and cavity-particle interactions are important, is postponed to a future work. An application in view is in particular the modeling of experiments of collective sedimentation and diffusion.

References

Beenakker, C. W. J.; Mazur, P. (1985): Is sedimentation container-shape dependent? *Phys. Fluids*, vol. 28, no. 11, pp. 3203–3206.

Berker, R. (1963): *Intégration des équations d'un fluide visqueux incompressible*, volume VIII/2 of *Handbuch der Physik*, pp. 1–384. Springer Verlag, 1963.

Beskos, D. E. (1998): *Introduction to Boundary Element Methods*. Elsevier Science Publishers.

Bhattacharya, S.; Bławzdziewicz, J.; Wajnryb, E. (2005): Hydrodynamic interactions of spherical particles in suspensions confined between two planar walls. *J. Fluid Mech.*, vol. 541, pp. 263–292.

Blake, J. R. (1971): A note on the image system for a stokeslet in a no-slip boundary. *Proc. Camb. Phil. Soc.*, vol. 70, pp. 303–310.

Blake, J. R. (1979): On the generation of viscous toroidal eddies in a cylinder. *J. Fluid Mech.*, vol. 95, no. 2, pp. 209–222.

Bonnet, M. (1999): *Boundary Integral Equation Methods for Solids and Fluids*. John Wiley & Sons Ltd.

Brenner, H. (1961): The slow motion of a sphere through a viscous fluid towards a plane surface. *Chemical Engineering Science*, vol. 16, pp. 242–251.

C. A. Brebbia, J. C. T.; Wrobel, L. C. (1984): *Boundary Element Techniques*. Springer-Verlag, Theory and Applications in Engineering, Berlin Heidelberg New York Tokyo.

Chaoui, M.; Feuillebois, F. (2003): Creeping flow around a sphere in a shear flow close to a wall. *Quart. J. Mech. Applied Math.*, vol. 56, no. 3, pp. 381–410.

Cichocki, B.; Felderhof, B. U.; Hinsen, K.; Wajnryb, E.; Bławzdziewicz, J. (1994): Friction and mobility of many spheres in Stokes flow. *J. Chem. Phys.*, vol. 100, pp. 3780–3790.

Cooley, M. D. A.; O'Neill, M. E. (1969): On the slow motion generated in a viscous fluid by the approach of a sphere to a plane wall or stationary sphere. *Mathematika*, vol. 16, pp. 37–49.

Dean, W. R.; O'Neill, M. E. (1963): A slow rotation of viscous liquid caused by the rotation of a solid sphere. *Mathematika*, vol. 10, pp. 13–24.

Debbech, A.; Elasmi, L.; Feuillebois, F. (2010): The method of fundamental solution for the creeping flow around a sphere close to a membrane. *ZAMM - Z. Angew. Math. Mech.*, vol. 90, pp. 920–928.

Domingez, J. (1993): *Boundary Elements in Dynamics*. Computational Mechanics Publications, Elsevier Applied Science.

Ekiel-Jeżewska, M. L.; Wajnryb, E. (2009): Hydrodynamic interactions between spherical particles in Stokes flow by the multipole method. In Feuillebois, F.; Sellier, A.(Eds): *Theoretical Methods for micro-scale viscous flows*. Transworld Research Network. ISBN:978-81-7985-400-4.

Faxen, H. (1922-1923): Die Bewegung einer starren Kugel langs der Achse eines mit zaeher Fluessigkeit gefuellten Rohres. *Arkiv for Matematik, Astronomi och Fysik*, vol. 17, no. 27, pp. 1–28.

Faxen, H. (1924): Der Widerstand gegen die Bewegung einer starren Kugel in einer zaehen Fluessigkeit, die zwischen zwei parallelen ebenen Waenden eingeschlossen ist. *Arkiv for Matematik, Astronomi och Fysik*, vol. 18, no. 29, pp. 1–53.

Feuillebois, F. (1989): Some theoretical results for the motion of solid spherical particles in a viscous fluid. In Hewitt, G. F.; Delhaye, J. M.; Zuber, N.(Eds): *Multiphase Science and Technology, volume 4*, pp. 583–798. Hemisphere Publishing Co, New York.

H. Rezayat, D. J. S.; Rizzo, F. J. (1986): On time-harmonic elastic-wave analysis by the boundary element method for moderate to high frequencies. *Comp. Meth. in Appl. Mech. Engrg.*, vol. 55, pp. 349–367.

Hancock, G. J. (1953): The self propulsion of microscopic organisms through liquids. *Proc. R. Soc. London A*, vol. 217, pp. 96–121.

Happel, J.; Brenner, H. (1991): *Low Reynolds number hydrodynamics*. Kluwer Academic Publishers, Dordrecht, Boston, London.

Jeffery, G. B. (1922): The motion of ellipsoidal particles immersed in a viscous fluid. *Proc. Roy. Soc. A.*, vol. 102, pp. 161–179.

Jones, R. (2004): Spherical particle in Poiseuille flow between planar walls. *J. Chem. Phys.*, vol. 121, no. 1, pp. 483–500.

Jones, R. (2009): Dynamics of a colloid in a spherical cavity. In Feuillebois, F.; Sellier, A.(Eds): *Theoretical Methods for micro-scale viscous flows*. Research Signpost, Trivandrum, India. In press.

Kim, S.; Karrila, S. (1991): *Microhydrodynamics: Principles and Selected Applications*. Butterworth-Heinemann.

Lecoq, N.; Masmoudi, K.; Anthore, R.; Feuillebois, F. (2007): Creeping motion of a sphere along the axis of a closed axisymmetric container. *J. Fluid Mech.*, vol. 585, pp. 127–152.

Liron, N.; Mochon, S. (1976): Stokes flow for a stokeslet between two parallel flat plates. *J. Eng. Math.*, vol. 10, no. 4, pp. 287–303.

Lorentz, H. A. (1897): A general theorem concernng the motion of a viscous fluid and a few consequency derived from it. *Versl. Kon. Acad. Wet. Amst.*, vol. 5, pp. 168–175. in german.

Lyness, J. N.; Jespersen, D. (1975): Moderate degree symmetric quadrature rules for the triangle. *J. Inst. Math. Appl.*, vol. 15, pp. 19–32.

Maude, A. D. (1961): End effects in a falling-sphere viscometer. *British J. of Appl. Physics*, vol. 12, pp. 293–295.

O'Neill, M. E. (1964): A slow motion of viscous liquid caused by a slowly moving solid sphere. *Mathematika*, vol. 11, pp. 67–74.

O'Neill, M. E. (1967): A slow motion of viscous liquid caused by a slowly moving solid sphere: an addendum. *Mathematika*, vol. 14, pp. 170–172.

O'Neill, M. E. (1968): A sphere in contact with a plane wall in a slow linear shear flow. *Chemical Engineering Science*, vol. 23, pp. 1293–1298.

O'Neill, M. E. (1969): On asymmetrical slow viscous flows caused by the motion of two equal spheres almost in contact. *Proc. Camb. Phil. Soc.*, vol. 65, pp. 543–555.

Pasol, L.; Chaoui, M.; Yahiaoui, S.; Feuillebois, F. (2005): Analytical solutions for a spherical particle near a wall in axisymmetrical polynomial creeping flows. *Phys. Fluids*, vol. 17, no. 7, pp. 073602.

Pasol, L.; Sellier, A. (2006): Gravitational motion of a two-particle cluster between two parallel plane solid walls. *C. R. Mécanique*, vol. 334, pp. 105–110.

Pasol, L.; Sellier, A.; Feuillebois, F. (2006): A sphere in a second degree polynomial creeping flow parallel to a wall. *Quart. J. Mech. Applied Math.*, vol. 59, pp. 587–614.

Pasol, L.; Sellier, A.; Feuillebois, F. (2009): Creeping flow around a solid sphere in the vicinity of a plane solid wall. In Feuillebois, F.; Sellier, A.(Eds): *Theoretical Methods for small scale viscous flows*. Transworld Research Network. ISBN: 978-81-7895-400-4.

Pozrikidis, C. (1992): *Boundary integral and singularity methods for linearized viscous flow*. Cambridge University Press.

Sano, O. (1987): Mobility of a small sphere in a viscous fluid confined in a rigid circular cylinder of finite length. *J. Phys. Soc. Japan*, vol. 56, no. 8, pp. 2713–2720.

Sano, O.; Hasimoto, H. (1976): Slow motion of a spherical particle in a viscous fluid bounded by two perpendicular walls. *J. Phys. Soc. Japan*, vol. 40, no. 3, pp. 884–890.

Sano, O.; Hasimoto, H. (1977): Slow motion of a small sphere in a viscous fluid in a corner. I. Motion on and across the bissector of a wedge. *J. Phys. Soc. Japan*, vol. 42, no. 1, pp. 306–312.

Sano, O. H. H. (1978): The effect of two plane walls on the motion of a small sphere in a viscous fluid. *J. Fluid Mech.*, vol. 87, pp. 673–694.

Sellier, A. (2007): Slow viscous migration of a conducting solid particle under the action of uniform ambient electric and magnetic fields. *CMES-Computer Modelling in Engineering & Sciences*, vol. 21, no. 2, pp. 105–132.

Sellier, A. (2008): Slow viscous motion of a solid particle in a spherical cavity. *CMES-Computer Modelling in Engineering & Sciences*, vol. 25, no. 3, pp. 165–179.

Shankar, P. (2007): *Slow viscous flows*. Imperial College Press, London.

Stokes, G. G. (1851): On the effect of the internal friction of fluids on the motion of pendulums. *Transactions of the Cambridge Philosophical Society*, vol. 9, pp. 8.

Stroud, A. H.; Secrest, D. (1966): Gaussian quadrature formulas. *Prentice-Hall*. Englewood Cliffs, N.J.

Vasseur, P.; Cox, R. G. (1976): The lateral migration of a spherical particle in two-dimensional shear flows. *J. Fluid Mech.*, vol. 78, pp. 385–413.

Youngren, G. K.; Acrivos, A. (1975): Stokes flow past a particle of arbitrary shape: a numerical method of solution. *J. Fluid Mech.*, vol. 69, no. 2, pp. 377–403.

Youngren, G. K.; Acrivos, A. (1976): Stokes flow past a particle of arbitrary shape: a numerical method of solution. Corrigendum. *J. Fluid Mech.*, vol. 75, pp. 813.